Crustal azimuthal anisotropy in the Jiaodong Peninsula: Evidence for the suture between the North China Craton and South China Block

Chenglong Wu [a], Tao Xu [a,b,*], Yinshuang Ai [b,c], Weiyu Dong [a,e], Long Li [c,e], Jue Hou [a,d,e]

[a] *State Key Laboratory of Lithospheric Evolution, Institute of Geology and Geophysics, Chinese Academy of Sciences, Beijing 100029, China*
[b] *Innovation Academy for Earth Science, Chinese Academy of Sciences, Beijing 100029, China*
[c] *Key Laboratory of Earth and Planetary Physics, Institute of Geology and Geophysics, Chinese Academy of Sciences, Beijing 100029, China*
[d] *Institute of Geophysics, China Earthquake Administration, Beijing 100081, China*
[e] *University of Chinese Academy of Sciences, Beijing 100049, China*

A B S T R A C T

The Jiaodong Peninsula is an ideal region for studying the geodynamics of collision between the North China Craton (NCC) and South China Block (SCB). It is comprised of the Jiaobei massif and the Northern Sulu UHP massif which are separated by the Wulian suture zone (WSZ). Continent-continent collision is necessarily accompanied with crustal deformation. Consequently a detailed crustal deformation pattern would offer observational constraints for understanding the process of the collision. In this study, we measured the crustal azimuthal anisotropy beneath a broadband seismic profile of 20 stations together with 9 permanent stations in the Jiaodong Peninsula. Sinusoidal moveout of Pms phases from radial receiver functions and azimuth-weighted stacking of transverse receiver functions were jointly applied to ensure the reliability of results. In the WSZ, the fast directions are roughly parallel with the NE oriented fault strike, suggesting the Jiaodong Peninsula may preserve fossilized anisotropy in the crust induced by the Triassic collision of the NCC and SCB although have undergone subsequent lithosphere destruction and thinning since the late Mesozoic. We therefore support that the WSZ represents the NCC-SCB suture east of Tanlu fault. In the Jiaobei massif, the crustal azimuthal anisotropy is controlled by both the nearly *E*-W local stress and NNE-strike detachment faults. The anisotropy beneath the Northern Sulu massif is quite weak with delay times all less than 0.20 s, probably related to the high-density UHP metamorphic rocks which are difficult to generate strong anisotropy inside.

1. Introduction

The Dabie-Sulu UHP orogenic belt separates the North China Craton (NCC) and South China Block (SCB) and formed during Triassic continent-continent collision (Fig. 1; Hacker et al., 1998, 2000). Thus it is a perfect region to study the geodynamics of continental subduction and exhumation. The orogenic belt is divided by NNE-string Tanlu fault (TLF) into two sections, the Qinling-Dabie orogen in the west and Sulu orogen in the east. It is generally accepted that the suture between NCC and SCB west of the TLF lies near the northern boundary of the Qinling-Dabie orogen (Okay and Celal Şengör, 1992). However, the east segment location of the NCC-SCB suture has been a subject of hot debate.

The Jiaodong Peninsula is located in the eastern boundary of the NCC, which primarily consists of the Jiaobei massif and Northern Sulu

UHP massif separated by the Wulian suture zone (WSZ). The Jiaobei massif in the northwest is mainly composed of Archean metamorphic rocks and Mesozoic granitic rocks (Yang et al., 2003a; Mao et al., 2008; Yang and Santosh, 2015), whereas the northern Sulu UHP massif in the southeast contains typical UHP metamorphic rocks. The WSZ is commonly assumed as the NCC-SCB suture in the Sulu orogen (Gilder et al., 1999; Zhai et al., 2000). Zircon U—Pb age and geochemical evidence show that the protoliths of UHP metamorphic rocks in the northern Sulu massif have a tectonic affinity to the SCB, like those rocks elsewhere along the Dabie-Sulu orogenic belt, suggesting the suture is located along the WSZ (Tang et al., 2008). The view was supported by zircon dating of Archean basement gneiss and the Penglai Group which implies that the Jiaobei massif has a NCC affinity (Zhou et al., 2008). By contrast, according to the similarities in petrological and structural
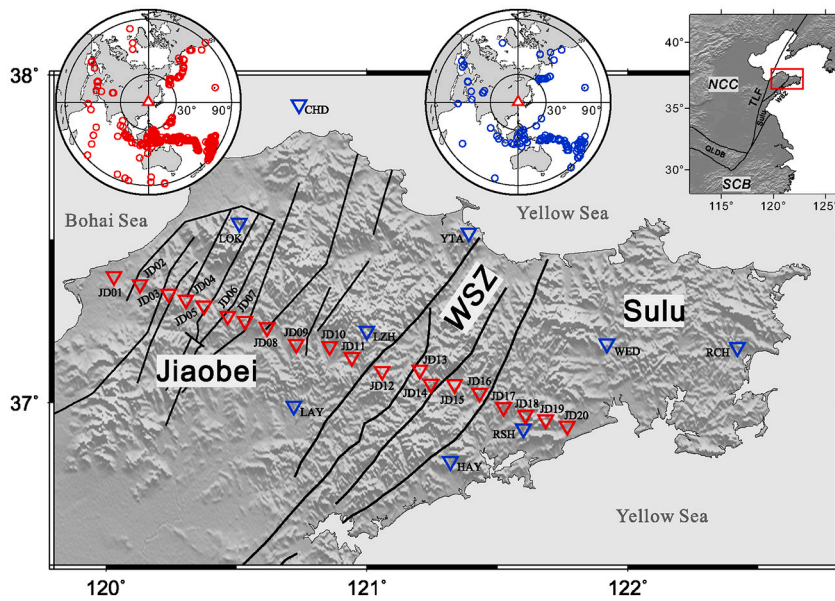

Fig. 1. Map of the Jiaodong Peninsula (eastern China). The study region is noted by the red rectangle in the upper right inset. The red triangles are the locations of seismic stations belong to the profile NCISP9. The blue triangles indicate permanent stations. Earthquake events used to calculate receiver functions are shown as small red and blue circles on a worldwide map in the upper part used by temporary and permanent stations respectively. Abbreviations: Jiaobei, Jiaobei massif; Sulu, Northern Sulu UHP massif; WSZ, Wulian suture zone; in the upper right inset: NCC, North China Craton; SCB, South China Block; QLDB, Qinling-Dabie orogenic belt and TLF, Tanlu fault. (For interpretation of the references to colour in this figure legend, the reader is referred to the web version of this article.)

features between the Jiaobei massif and Northern Sulu massif, Faure et al. (2001) argued that the NCC-SCB suture should lie north of the Jiaobei massif. Considering the Wulian granitoids as tectonic slices scraped off from the upper part of the subducting SCB by the NCC obduction, Wu et al. (2004) and Zheng et al. (2005) likewise proposed that the suture might be placed north of the Wulian and Penglai groups rather than along the WSZ.

In recent years, some geophysical observations have been carried out in the Jiaodong Peninsula (Chen et al., 2006; Zheng et al., 2008; Pan et al., 2015; Li et al., 2018; Zhang et al., 2018; Yu et al., 2020a, 2020b). Receiver function imaging, deep seismic sounding investigations and the deep electrical model of one MT profile all revealed that the WSZ is a steep transcrustal fault (Yu et al., 2020a; Pan et al., 2015; Zhang et al., 2018). Seismic azimuthal anisotropy observations could record the deformation of crust and mantle related to the continent-continent collision. The XKS splitting analysis of a WNW-ESE seismic array showed that there exists a double-layer anisotropic structure beneath the WSZ (Wu et al., 2020). The lower layer oriented in WNW-ESE is roughly parallel with the single-layered anisotropy of the Jiaobei massif and Northern Sulu massif, as well as previous observations (Tian and Santosh, 2015; Shi et al., 2015), and the anisotropy likely stems from asthenospheric flow. The upper layer exhibits a NE oriented fast direction parallel to the WSZ strike, implying that the lithosphere may preserve fossilized anisotropy induced by the Triassic collision of the NCC and SCB. However, one of the main disadvantages of XKS splitting analysis is the lack of vertical resolution despite that the olivine alignment in the upper mantle dominates the observed waveforms (Savage, 1999). In comparison, the P-to-S converted wave at the Moho is strictly confined in the crust and conducive to offer valuable knowledge about the crustal deformation (Chen et al., 2013). The Pms phase, which can be extracted from receiver function, is now extensively applied to estimate seismic anisotropy in the crust (Liu and Niu, 2012; Kong et al., 2016; Wu et al., 2019a; Yang et al., 2019). In the regions which experienced complex deformational processes such as Tibet, a harmonic-decomposition technique was applied to obtain layered anisotropy distributed at various levels within the crust (Liu and Park, 2017; Liu et al., 2015). There haven't any investigations of the crustal azimuthal anisotropy based on Pms arrival variation in the Jiaodong Peninsula till now however.

In this study, we estimated the crustal azimuthal anisotropy to study the crustal deformation of the Jiaodong Peninsula, and provided more constraints for the suture location between the NCC and SCB. We took advantage of the teleseismic events from a WNW-ESE linear seismic profile and some permanent stations to calculate receiver functions. The splitting parameters including fast polarization direction and delay time were measured by the sinusoidal moveout of Pms phases from radial receiver functions. In addition, we used the azimuth-weighted stacking of transverse receiver functions (AWST) to determine the fast direction. The two techniques were exploited jointly to estimate the crustal azimuthal anisotropy.

2. Data and method

2.1. Receiver function

The data used in this study were collected from the linear seismic profile NCISP9 deployed from 2017 November to 2019 August (Wu et al., 2020). The profile was WNW-ESE striking across the WSZ and included 20 broad-band stations (Fig. 1). The total length of the profile is 170 km with an average spacing of 9 km. To increase data coverage in the Jiaodong Peninsula, we used additional recordings from nine permanent stations close to the profile. They belong to the China National Seismic Network and were recorded from 2017 March to 2018 September (Zheng et al., 2010). We selected the data of teleseismic events with magnitude larger than 5.5 and epicentral distances of 30–90°. Prior to calculate receiver functions, we corrected the sensor misorientation using P-wave particle motion (see Wu et al., 2020 for more details). The stations with an estimated deviation azimuth greater than 7° were corrected for the reason that the smaller deviation could be also caused by near station structure besides sensor misorientation (Niu and Li, 2011).

The original data were band-pass filtered for 0.01–1 Hz. Records with high SNR and clear arrival of P waves were chosen. We rotated the two horizontal components into radial-transverse (R-T) coordinate system. The time-domain iterative deconvolution technique was employed to generate radial and transverse receiver functions, abbreviated as RRFs and TRFs (Ammon, 1991). A low-pass Gaussian filter with a width factor of 2.5 Hz was applied to regulate the deconvolution. All the receiver functions were checked visually, and those with unclear Pms arrivals were discarded. We finally gathered 3691 pairs of R and T receiver functions. In order to eliminate the dependence of arrival time on epicentral distance, all the RFs were moveout corrected with a reference horizontal slowness $p = 6.4$ s/deg. using the IASP91 model (Kennett and Engdahl, 1991).

Table 1
velocity model of anisotropic crust with flat Moho.

Model1	Thickness /m	Density /(kg*m⁻³)	Iso	Vp /(m*s⁻¹)	Vs /(m*s⁻¹)	%P	%S	Trend (°)	Pl	St	Di
Layer1	20,000	2600	1	5800	3800	0	0	0	0	0	0
Layer2	30,000	2900	0	7000	4000	10	10	60	0	0	0
Layer3	∞	3500	1	8100	4500	0	0	0	0	0	0

Iso is the mark of anisotropy, 1 or 0 means the layer is isotropic or anisotropic;
%P and %S denote anisotropy magnitude;
Trend and Pl denote fast direction and dip angle respectively;
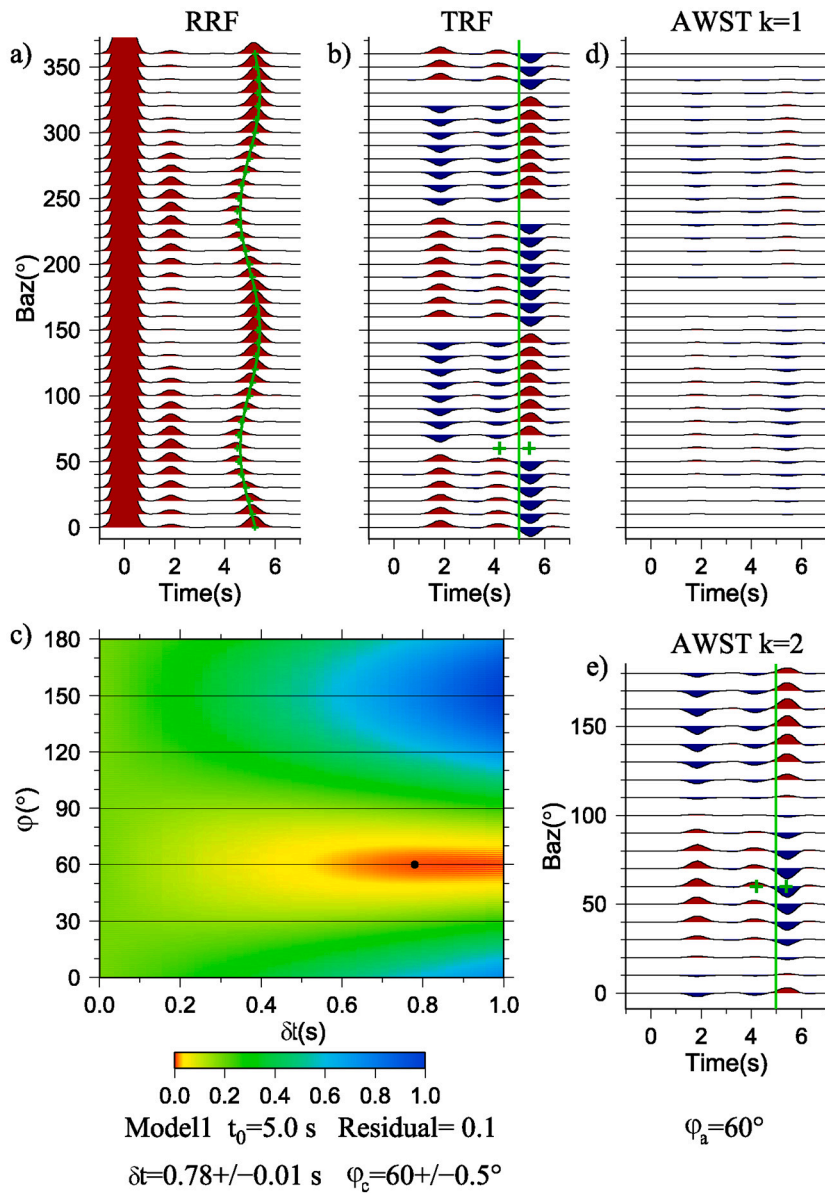St and Di denote interface strike and dip angle respectively.

Fig. 2. Synthetic receiver functions of Model 1 (flat Moho, Table 1) and AWST section. (a) RRFs. The green line represents the Pms arrival with π periodicity predicted by the anisotropic model. (b) TRFs. The green crosses indicate the azimuth of the polarity reversal, which corresponds to the fast direction. (c) surface map of normalized R value. The black dot denotes the optimal pair of splitting parameters corresponding to the minimum R value. (d) AWST section with k = 1. (e) AWST section with k = 2. The green crosses mark the maximum stacking amplitude and minimum amplitude produced by the lower interface of the anisotropic layer, and the corresponding backazimuth is equal to the fast direction of 60°. The green line represents t_0. Fast direction φ_c, delay time δt, t_0 and R value between observed and best predicted Pms arrivals for RRFs, fast direction φ_a for AWST are listed in the bottom. (For interpretation of the references to colour in this figure legend, the reader is referred to the web version of this article.)

2.2. Detection of single layered anisotropy by receiver functions

Numerous studies have investigated crustal azimuthal anisotropy utilizing receiver functions including splitting of P to S conversions from the Moho (Chen et al., 2013; Qiang et al., 2016), and azimuthal variation of P to S conversions (Liu and Niu, 2012; Wang et al., 2016; Sun et al., 2012; Wu et al., 2019a). The latter technique has been applied more frequently in recent years as it could overcome the instability of analysis from individual event.

A model with one horizontal anisotropic layer (velocity anisotropies of 10%) in the crust is shown in Table 1. We used the raysum program (Frederiksen and Bostock, 2000) to generate synthetic seismograms and calculated R and T receiver functions which were shown as a function of backazimuth (Fig. 2a and b). Because Pms arrival times in the study region are mainly $4.0 \pm 0.2\,\text{s}$, we assumed that the variation of Pms arrival times is caused by a single anisotropic layer with horizontal symmetry.

Assuming a single anisotropic layer with horizontal symmetry, the Pms arrival time varies systematically with the backazimuth of the earthquake (Liu and Niu, 2012; Rümpker et al., 2014) and could be expressed as:

$$t_{Pms} = t_0 - \frac{\delta t}{2} cos[2(\alpha - \varphi_c)], \tag{1}$$

where t_0 represents the Pms arrival time in isotropic case, δt is the delay time between the fast and slow waves which mirrors the strength of anisotropy, and φ_c denotes the fast polarization orientation; α is the backazimuth of the earthquake event. The green line in Fig. 2a shows the theoretical Pms arrival times based on formula (1) fitting well with the variation of observed Pms arrivals. When processing with field data, we stacked the RFs in the same BAZ band of $10°$ wide to avoid the uneven BAZ distributions of earthquake events. A grid research was performed to obtain the optimal pair of splitting parameters that corresponds to the minimum difference between observed and predicted arrival times. We introduced R value, which is the square norm of the residual between observed and optimal predicted Pms arrivals, to evaluate the quality of Pms arrival fitting. The searching range for t_0 is 3.0–5.0 s with an increment of 0.1 s, and those for φ_c and δt_c are 0–180° with a step of 1°, 0–1.0 s with a time interval of 0.01 s, respectively. Fig. 2c shows the surface map of normalized R value, and the value reaches minimum at theoretical splitting parameters. To quantify the uncertainties of the splitting parameters, we adopt the bootstrap resampling method to estimate the splitting parameters 10 times and obtain err_φ and $err_{\delta t}$ which are standard deviations (SD) of φ_c and δt_c respectively.

The crustal anisotropy parameters could be constrained by TRFs as well. The phases around 5.0 s produced by the lower interface of the anisotropic layer exhibit the polarity reversal indicated by the green crosses in Fig. 2b which correspond to the fast direction of the anisotropic layer. It seems a simple means to obtain the fast direction by finding the location of polarity reversal in TRFs. However the method is effective in case that there is a sufficient coverage of backazimuth and the anisotropic structure is not complex, which is not usually met when dealing with field data. A more robust method called AWST has been successfully applied in northeast Tibet and Inner Mongolia (Shen et al., 2015; Qiang et al., 2019). In this study we determined the fast direction with the help of AWST method.

Girardin and Farra (1998) constructed the AWST section by stacking the TRFs with different weighting coefficients related to backazimuth to extract the anisotropic signal in the records. The AWST section is expressed as,

$$S_T(k, t, \varphi_a) = \sum_{i=1}^{n} W_i^T(k, \varphi_a) T_i(t), \tag{2}$$

$$W_i^T(k, \varphi_a) = \frac{sink(\varphi_a - \alpha_i)}{\sum_{j=1}^{n} sin^2 k(\varphi_a - \alpha_j)}, \tag{3}$$
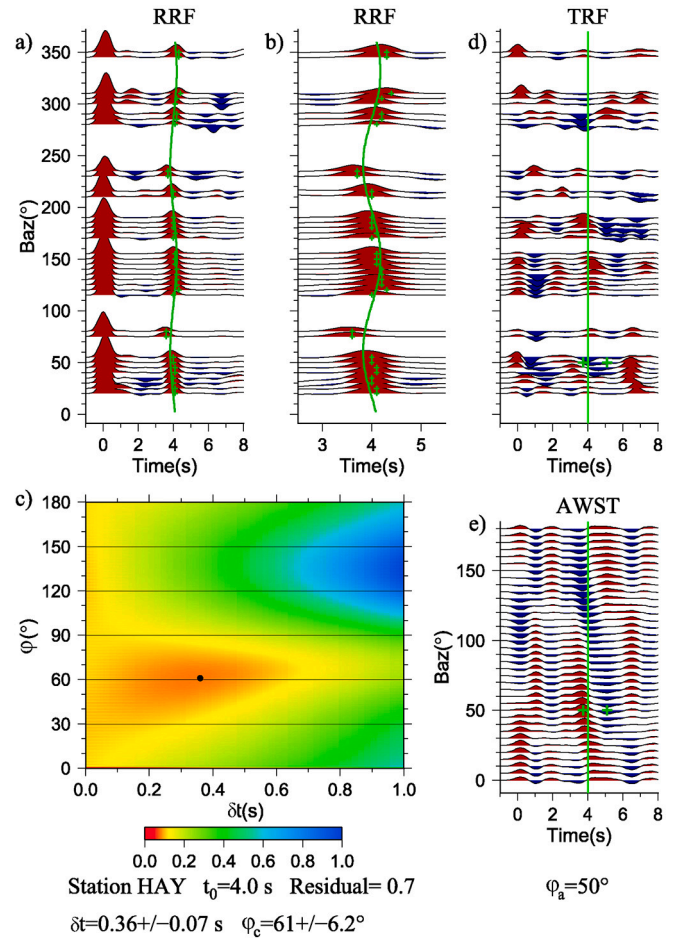

Fig. 3. Observed receiver functions and AWST section of station HAY. (a) RRFs. Small green crosses mark the Pms arrivals. The green line represents the Pms arrivals predicted by the optimal splitting parameters. (b) Zoomed-in RRFs in a narrow time window to have a clear view of Pms arrival variation. (c) surface map of normalized R values. The black dot denotes the optimal pair of splitting parameters corresponding to the minimum R value. (d) TRFs. The green line represents t_0. Green crosses mark the fast direction determined by AWST method in subfigure e. (e) AWST method with $k = 2$. The green line represents t_0. The green crosses mark the maximum/minimum stacking amplitudes produced by the lower interface of the anisotropic layer, and the corresponding backazimuth indicates the fast direction. Station name, t_0, fast direction φ_c, delay time δt and R value between observed and best predicted Pms arrivals for RRFs, fast direction φ_a for AWST are listed in the bottom. (For interpretation of the references to colour in this figure legend, the reader is referred to the web version of this article.)

where, $T_i(t)$ is the individual TRF trace, k is the harmonic order, φ_a is a variable angle, α_i is the backazimuth of the ith event. When φ_a is equal to the fast direction, the AWST section S_T reaches the maximum amplitude and minimum amplitude around the lower interface of the anisotropic layer. Synthetic stacking results with $k = 1$ and $k = 2$ are shown in Fig. 2d and e. Fig. 2e only shows the data from 0 to 180° because the AWST section with $k = 2$ has a period of π. Fig. 2d shows significantly weak amplitude with $k = 1$, and maximum and minimum amplitudes could not be picked at the angle of fast direction from the AWST section. The AWST with $k = 2$ shows maximum and minimum amplitudes around 5.0 s at the correct fast direction of 60° in Fig. 2e. Previous studies found that the AWST with $k = 2$ performs better to the azimuthal anisotropy and even with a dipping symmetry axis by testing different k values (Girardin and Farra, 1998; Shen et al., 2015; Qiang et al., 2019). Therefore, we estimated the fast direction by applying AWST with $k = 2$. The maximum and minimum amplitudes around the lower interface of
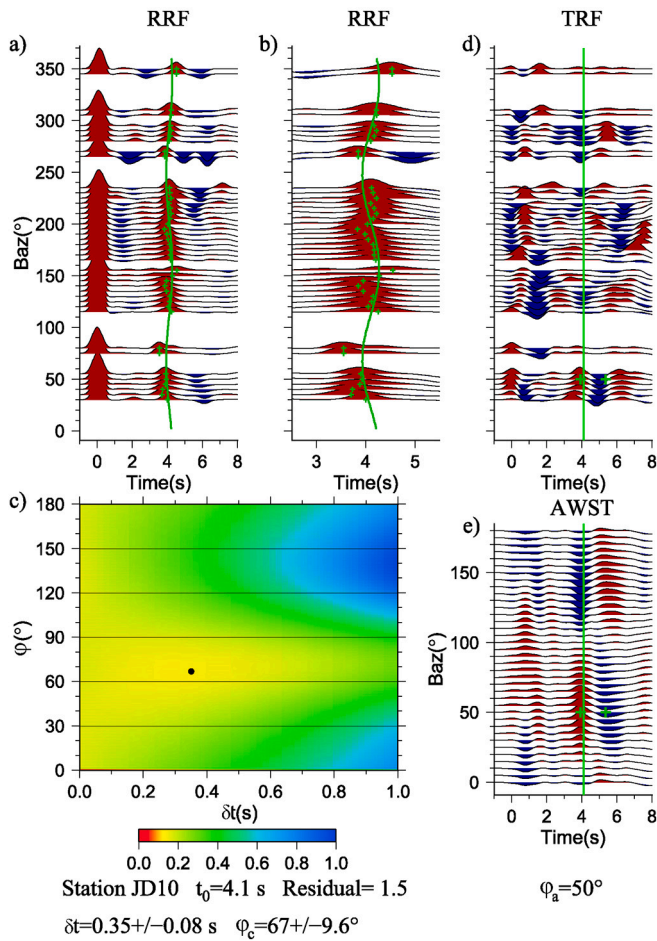
Fig. 4. Same as Fig. 3 except for station JD10.

Fig. 5. Same as Fig. 3 except for station JD05. The gray line in Fig. 5b marks the Pms arrival curve predicted by the fast direction determined by AWST method in Fig. 5e. The theoretical Pms arrival curve predicted by AWST disagrees with the observed Pms arrivals marked by the small green crosses. (For interpretation of the references to colour in this figure legend, the reader is referred to the web version of this article.)

anisotropic layer appear in a symmetric pair, but it might be difficult to inspect them together in field data. We sought the strongest signal around Pms to estimate the fast directions in practice.

In this study we combined the two methods to estimate the splitting parameters. Results from arrival time fitting is more stable as the SNR of Pms phases in RRFs is much higher than that in TRFs. We obtained the fast directions and delay times from RRFs, and the fast directions by AWST from TRFs were treated as a reference. We eliminated the results with R value greater than 2.0 which probably were influenced by complicated anisotropic structure. For results with R value less than 2.0, the difference between fast directions from Pms arrival fitting and AWST methods should be less than 25°. If the discrepancy angle exceeds 25°, we only preserved the results from RRFs with R value no more than 1.0.

Recent studies show that the Moho topography, i.e., dipping Moho may cause azimuthal variation of the Pms delays (Li et al., 2019; Wang et al., 2020). To test the influence on the splitting parameters, we obtained Moho depth from H-κ scanning results (Fig. S1, from Yu et al., 2020a and their unpublished results). The Moho is approximately flat with average depth 33.1 ± 2.0 km, and dip angle is less than 5°. We designed the anisotropic Model 2 with 10° dipping Moho (Table S1). The two methods both got consistent results with the theoretical splitting parameters, but larger error values than those for Model 1 (Fig. S2), which demonstrates that our method is applicable in the study region.

3. Results

Most stations show a period of π except station JD14 with R value more than 2.0, indicating that a single anisotropic layer with a horizontal symmetric axis is the main cause for variation of RFs. Here we
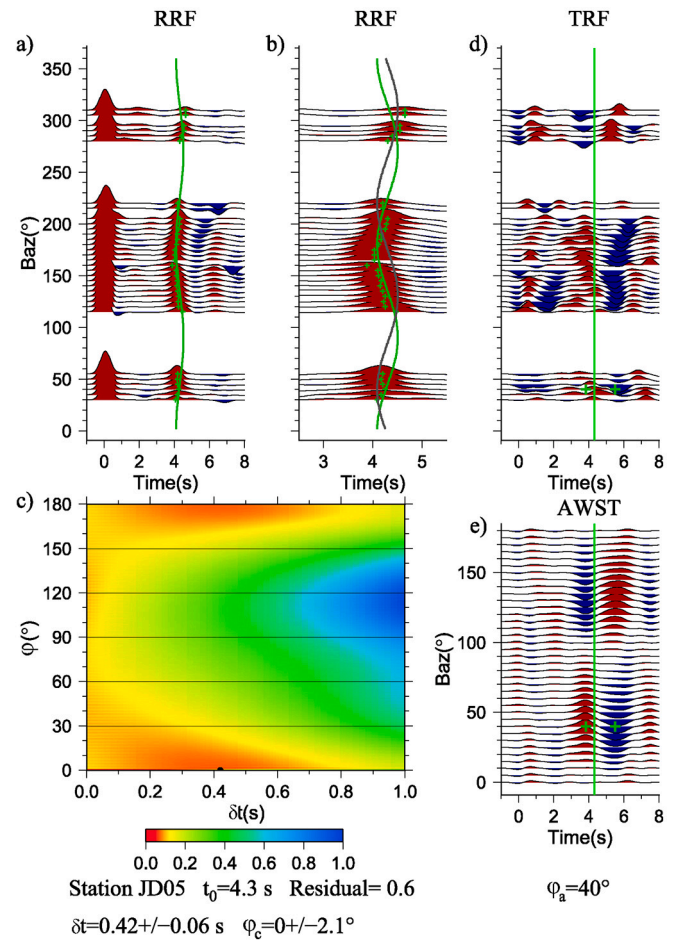
perform the analysis of different types of our measurements by exploiting the combination of RRFs and TRFs.

At permanent station HAY, we selected 77 high-quality pairs of RFs and stacked traces within 10° backazimuthal bins. The number of available BAZ bands is 36 out of 72 possible bands. The Pms phases appear around 4.0 s in RRFs (Fig. 3a). A clear backazimuthal variation of Pms arrival times can be observed with a period of π. We performed a grid search to obtain the optimal pair of splitting parameters, which includes $t_0 = 4.0$ s, $\varphi_c = 61°$ and $\delta t = 0.36$ s. The R value is 0.7 suggesting the theoretical Pms arrival times generated from the splitting parameters fit well with the observed arrival times (Fig. 3b). R value reaches minimum at the optimal splitting parameters (Fig. 3c). The polarity reversal in the TRFs seems to be located at 35° (Fig. 3d). However it is difficult to determine the fast direction in this way due to the indistinct variation of polarity. The AWST analysis shows that the fast direction is 50° where the maximum and minimum amplitudes appear in a symmetric pair around 4.0 s (Fig. 3e). The consistence of the two methods from RRFs and TRFs respectively confirms the reliability of the splitting parameters.

At temporary station JD10 we got similar results as station HAY. By fitting Pms arrival times in the RRFs we obtained the optimal pair of parameters including $\varphi_c = 67°$, $\delta t = 0.35$ s, and $t_0 = 4.1$ s (Fig. 4a, b, c). We cannot observe the polarity reversal in the vicinity of φ_c in the TRFs (Fig. 4d), whereas the AWST section shows paired maximum and
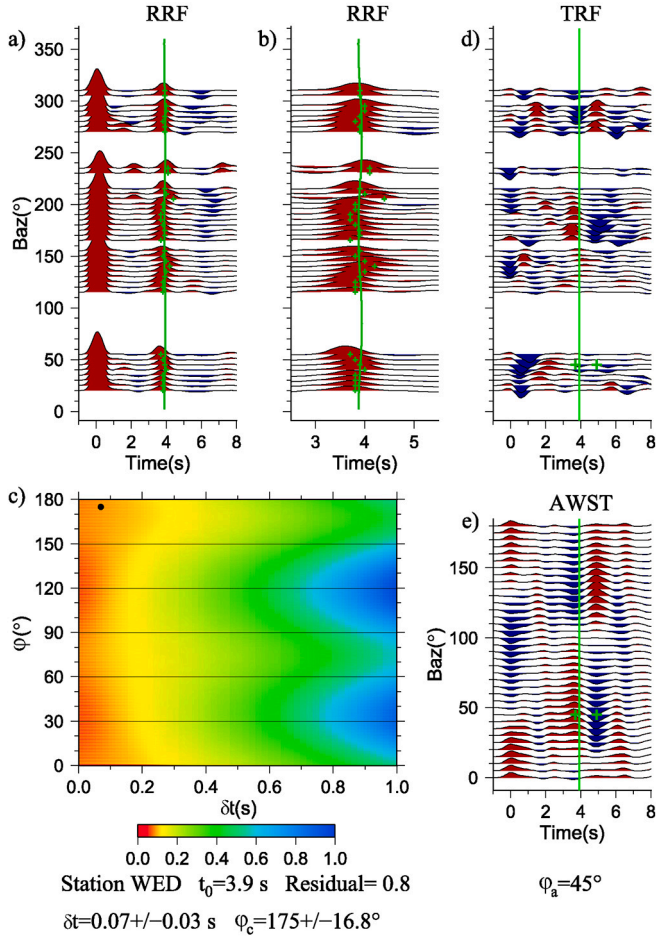
Fig. 6. Same as Fig. 3 except for station WED.

Fig. 7. Same as Fig. 3 except for station JD20.

minimum amplitudes around 4.1 s at 50° corresponding to φ_a, which is approximately consistent with φ_c (Fig. 4e). The pair of splitting parameters is accepted owing to the coherence between φ_c and φ_a.

At station JD05, we determined the splitting parameters $\varphi_c = 0°$, $\delta t = 0.42$ s by modelling Pms time variation (Fig. 5). However, the AWST method estimated the fast direction φ_a of 40°. There is not a distinct polarity reversal in the TRFs. We calculated the theoretical Pms arrival curve based on formula (1) with $\varphi_a = 40°$ which cannot well fit the primary variation tendency of observed arrival times (Fig. 5b). In this case we chose the results obtained by RRFs with R value no more than 1.0.

For stations with weak anisotropy, i.e., $\delta t < 0.2$ s, the error range is generally quite large and it is difficult to generate consistent fast directions by RRFs and TRFs respectively. We determined the splitting parameters based on better fitting of Pms arrival times in RRFs with R value no more than 1.0. For example, at permanent station WED a discrepancy exists about 50° between the fast directions by the two methods (Fig. 6). We chose the parameters $\varphi_c = 175°$, $\delta t = 0.07$ s with $R = 0.8$ as the final results. Fig. 7 shows the similar case at temporary station JD20. The splitting parameters from RRFs are deemed acceptable.

Finally except station JD14 with R value greater than 2.0, the other stations are classified into three categories (Figs. S3-S25, Table 2). Similar to stations HAY and JD10, stations LAY, LOK, LZH, YTA, JD02,
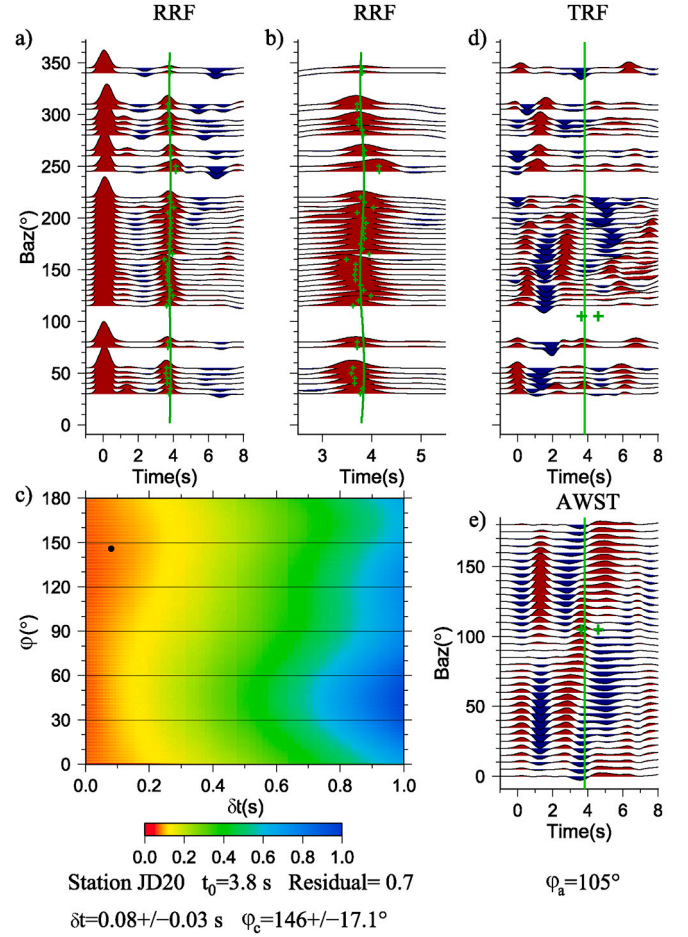
JD03 and JD11 have consistent results by the two method. Stations CHD, JD01, JD12 and JD17 belong to the kind of station JD05. For the left 13 stations, they are the same cases with station WED and show weak anisotropy. The distribution of fast directions is relatively discrete, while that of delay times is mainly concentrated around 0.20 s (Fig. 8). The spatial distribution of angular differences are shown in Fig. S26. The detailed anisotropy parameters beneath 28 stations are listed in Table 2 and shown in Fig. 9.

4. Discussion

Anisotropy of the upper crust is generally attributed to dilatancy of micro-cracks producing a fast direction parallel to the maximum horizontal compressive stress (S_{Hmax}) (Crampin, 1991). Such stress-induced anisotropy is most remarkable in the near surface, and the effect decreases with depth as the confining pressure increases, causing micro-cracks in all orientations to close (Boness and Zoback, 2006). Alternatively, anisotropy within the crust can also be produced by aligned macroscopic fractures associated with regional tectonics, fault-zone fabrics and aligned minerals and/or grains, which cause the S-waves to be polarized along a fast direction within planes defined by the feature. These types of anisotropy are collectively referred to as structural anisotropy (Boness and Zoback, 2006).

Most studies regard observed crustal anisotropy as a combination of

Table 2
The measurements of crustal azimuthal anisotropy.

Station	Latitude (°)	Longitude (°)	Residual	t_0 (s)	δt_c (s)	$err_{\delta t}$ (s)	φ_c (°)	err_φ (°)	φ_a (°)	Number
JD01	37.39	120.03	0.9	4.0	0.56	0.04	68	2.7	10	90
JD02	37.36	120.13	1.0	4.1	0.26	0.05	24	6.1	40	245
JD03	37.33	120.24	0.6	4.1	0.20	0.03	44	3.9	55	182
JD04	37.32	120.31	0.4	4.1	0.10	0.03	16	9.4	–	167
JD05	37.30	120.38	0.6	4.3	0.42	0.06	0	2.1	40	132
JD06	37.27	120.47	0.3	4.0	0.13	0.03	165	8.5	–	216
JD07	37.25	120.53	0.2	4.0	0.14	0.02	173	7.8	–	128
JD08	37.23	120.62	0.7	3.9	0.13	0.03	139	8.8	–	131
JD09	37.18	120.73	0.6	4.0	0.03	0.06	74	24	–	148
JD10	37.17	120.86	1.5	4.1	0.35	0.08	67	9.6	50	188
JD11	37.14	120.94	1.4	4.0	0.20	0.03	43	10.3	60	112
JD12	37.10	121.06	0.8	4.1	0.25	0.08	42	11	150	126
JD13	37.10	121.20	0.6	4.2	0.17	0.02	86	4.4	–	170
JD15	37.06	121.34	0.9	4.0	0.14	0.05	35	6.4	–	208
JD16	37.03	121.43	1.0	4.1	0.07	0.05	84	23.1	–	142
JD17	36.99	121.52	1.0	3.9	0.22	0.04	102	7.2	50	126
JD18	36.96	121.61	0.9	3.8	0.15	0.04	79	9.3	–	135
JD19	36.95	121.69	0.8	3.8	0.14	0.06	67	17.6	–	157
JD20	36.93	121.77	0.7	3.8	0.08	0.03	146	17.1	–	196
CHD	37.91	120.74	1.2	3.9	0.22	0.07	71	7.9	120	83
HAY	36.82	121.32	0.7	4.0	0.36	0.07	61	6.2	50	77
LAY	36.99	120.72	1.3	4.2	0.36	0.09	99	3.4	115	80
LOK	37.55	120.51	0.8	3.9	0.36	0.03	91	1.1	80	97
LZH	37.22	121.00	0.9	4.1	0.24	0.03	44	8.2	65	77
RCH	37.17	122.42	0.6	3.6	0.10	0.03	0	12.9	–	102
RSH	36.92	121.60	1.0	3.9	0.19	0.04	65	4.9	–	85
WED	37.18	121.92	0.8	3.9	0.07	0.03	175	16.8	–	89
YTA	37.52	121.39	0.9	3.8	0.30	0.05	86	4.9	70	85

t_0 represents the Pms arrival time in isotropic case;
Residual (R value) denotes square norm of residual between observed and theoretical Pms arrivals predicted by the optimal splitting parameters;
δt_c and φ_c denote the splitting parameters obtained by fitting Pms arrivals;
$err_{\delta t}$ and err_φ are standard deviations (SD) of δt_c and φ_c respectively;
φ_a is the fast direction obtained by AWST method;
Number indicates the number of pairs of receiver functions used to measure crustal azimuthal anisotropy.

stress-induced, structural anisotropy (Peng and Ben-Zion, 2004; Gao et al., 2011; Cochran and Kroll, 2015; Guo et al., 2015; Li and Peng, 2017). For example, Wu et al. (2019a, 2019b) conducted the SWS analysis of local S and Pms phases to investigate the crustal anisotropy in central Tibet. They found that both the conjugate strike-slip faults and local stress contribute to upper crustal anisotropy. The crustal flow results in lattice preferred orientation of anisotropic minerals and produces the anisotropy in lower crust. In the northern boundary of NCC near our study region, Yang et al. (2018b) and Zheng et al. (2019) revealed that NW-SE lithospheric extension since the late Mesozoic, active faults and EN*E*-WSW trending local stress play major roles in crustal anisotropy.

To facilitate analysis, we divided the stations into three segments according to their locations. The WSZ contains the stations JD10–17, LZH and HAY. The stations west of WSZ belong to the Jiaobei massif, and the ones east of WSZ are attached to the Sulu massif (Fig. 9). In WSZ, the average fast direction is parallel with the NE-strike of WSZ, which agrees well with the upper layer fast direction of the two-layer anisotropy pattern obtained by XKS splitting analysis (Wu et al., 2020). The crustal anisotropy is likely related to the Triassic collision of the NCC and SCB. This event may lead to coherent vertical deformation between the crust and lithospheric mantle at the suture zone and produce LPO of anisotropic minerals which lay along the NCC-SCB suture. The average delay time is 0.24 s and occupies about half of the upper layer delay time (0.50 s), suggesting that the crust and lithospheric mantle probably experienced comparative degree of deformation. Later the WSZ undergone a left strike-slip compression in the Late Jurassic

and a right strike-slip stretch in the Paleogene (Zhang et al., 2007). Shearing effects with these processes would strengthen the strike-parallel anisotropy. Besides, in the late Mesozoic, large-scale destruction occurred in the eastern NCC primarily caused by the subduction of the Paleo-Pacific plate (Zhu et al., 2004; Yang et al., 2005; Zhu and Zheng, 2009; Chen, 2010; Lin and Wei, 2020; Yang et al., 2018a; Meng and Lin, 2021). Nevertheless, the remnant lithosphere still preserved the fossilized anisotropy due to the NCC-SCB collision. The fast directions of stations JD13, JD16 and JD17 deviate from the fault strike to some degree, implying the complicated crustal deformation of the WSZ. The receiver function imaging of a dense linear array in the study region shows that there are significant differences between the opposite sides of the WSZ in terms of crustal structure, Moho depth, intracrustal LVZ and upper crustal Vp/Vs ratio, suggesting that the WSZ is a steep transcrustal fault (Yu et al., 2020a). Pan et al. (2015) also found that the crustal velocity structures appear different on either side of WSZ from a wide-angle reflection study. With regard to Faure et al. (2001), the structural analysis could only capture upper crustal deformation which contradicts with the deeper crustal deformation pattern in this study. We accordingly support that the WSZ represents the suture between the NCC and SCB east of the TLF.

In the Jiaobei massif, observations of S_{Hmax} from focal mechanisms, overcoring and well-bore data are oriented WNW-ESE or *E*-W (Heidbach et al., 2018). The fast directions of the stations LOK, CHD, YTA and LAY lie approximately E-W direction which are roughly parallel to S_{Hmax}, indicating that the crustal anisotropy beneath these stations is mainly attributed to aligned micro-cracks due to stress. In comparison, the
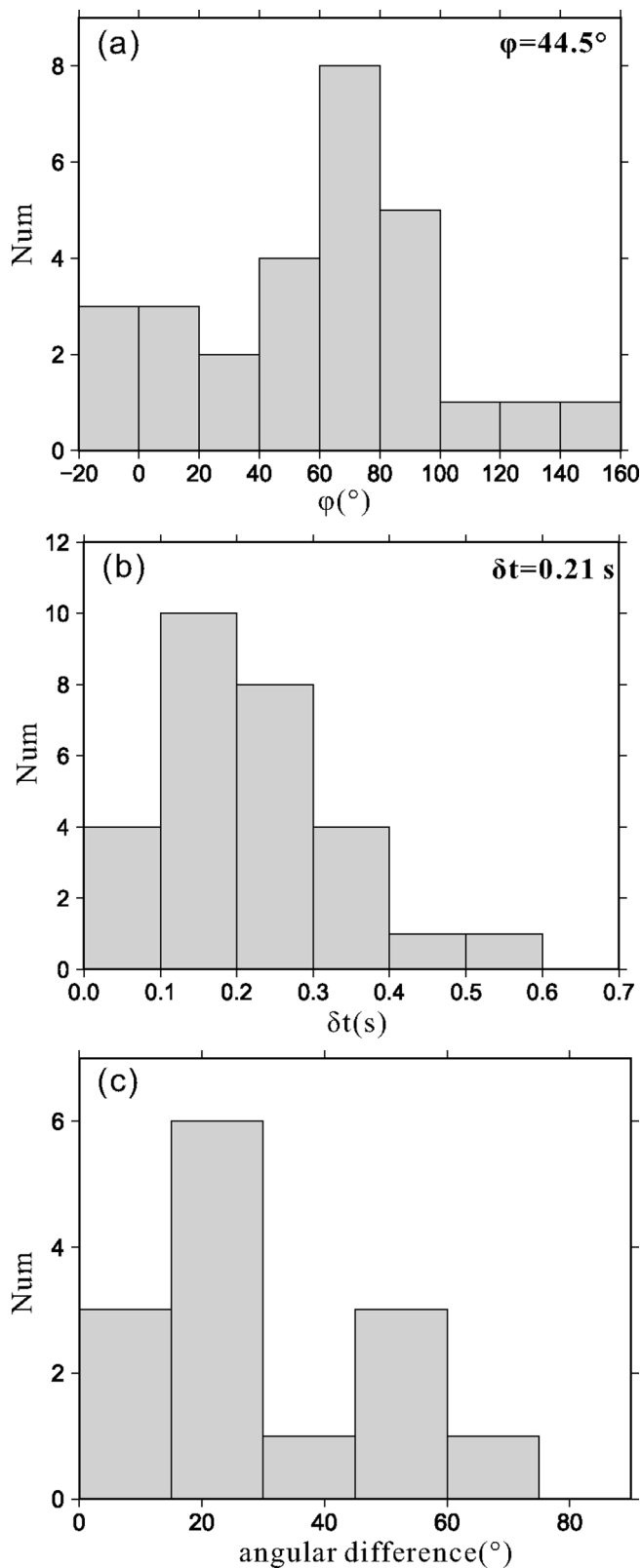
anisotropy of stations JD02-JD07 exhibits nearly N-S direction which is orthogonal to S$_{Hmax}$ direction, and JD01 shows NE oriented anisotropy. The fast directions are subparallel to the large-scale NNE-strike detachment faults which control the super-large gold deposits in this area, indicating that the anisotropy is caused by aligned macroscopic fractures along the faults. In particular, the thick crust-mantle boundary zones beneath the Jiaobei massif detected by receiver function analysis indicates a secular interaction between the crust and the underlying mantle, and implies magmatic underplating has occurred since the late Mesozoic (Yu et al., 2020a), which is supported by the study of Guojialing granodiorites (Yang et al., 2003b, Fig. 9b). The large delay times (>0.40 s) of stations JD01 and JD05 may be related to the magmatic underplating which would cause strong anisotropy in the lower crust.

The delay times of stations in the Northern Sulu UHP massif are all less than 0.20 s, suggesting the anisotropy is quite weak. The UHP metamorphic rocks undergone multiple stage exhumations from early to late stage of the collision and were distributed widely in the Sulu massif (Lin et al., 2013). The S-wave velocity of the upper crust by ambient noise tomography from a dense linear profile shows higher velocity of the Sulu massif than that of the Jiaobei massif likely due to the distribution of high-density UHP eclogites (Yu et al., 2020b). Thus the massif is so hard that it is difficult to generate strong deformation and related crustal anisotropy inside. The receiver function imaging also confirms the observation and shows that the interfaces in the crust of the Sulu massif are much flatter than adjacent regions (Yu et al., 2020a).

5. Conclusions

We estimated the crustal azimuthal anisotropy in the Jiaodong Peninsula from a WNW-ESE oriented seismic profile and some permanent stations to provide constraints for the suture location between the North China Craton and South China Block. We combined sinusoidal moveout of Pms phases from radial receiver functions and azimuth-weighted stacking of transverse receiver functions to determine the splitting parameters. In the Wulian suture zone, the fast directions agree well with NE oriented fault strike, indicating that the crust may preserve fossilized anisotropy induced by the Triassic collision between the NCC and SCB. We therefore support that the WSZ should be the NCC-SCB suture east of the Tanlu fault. In the Jiaobei massif, the crustal anisotropy is dominated by both the roughly E-W oriented local stress and NNE-strike detachment faults, whereas the anisotropy in the Northern Sulu massif is quite weak, probably related to the high-density UHP metamorphic rocks which are difficult to generate strong deformation and related anisotropy inside.

Supplementary data to this article can be found online at https://doi.org/10.1016/j.pepi.2021.106705.

CRediT authorship contribution statement

Chenglong Wu: Formal analysis, Methodology, Software, Visualization, Writing - original draft. **Tao Xu:** Conceptualization, Funding acquisition, Investigation, Writing - review & editing, Supervision. **Yinshuang Ai:** Investigation, Writing - review & editing. **Weiyu Dong:** Data curation, Investigation . **Long Li:** Data curation, Investigation . **Jue Hou:** Data curation, Investigation.

Declaration of Competing Interest

The authors declare that they have no known competing financial interests or personal relationships that could have appeared to influence the work reported in this paper.

Fig. 8. Histograms of fast directions (a), delay times (b) and angular differences by the two methods (c).
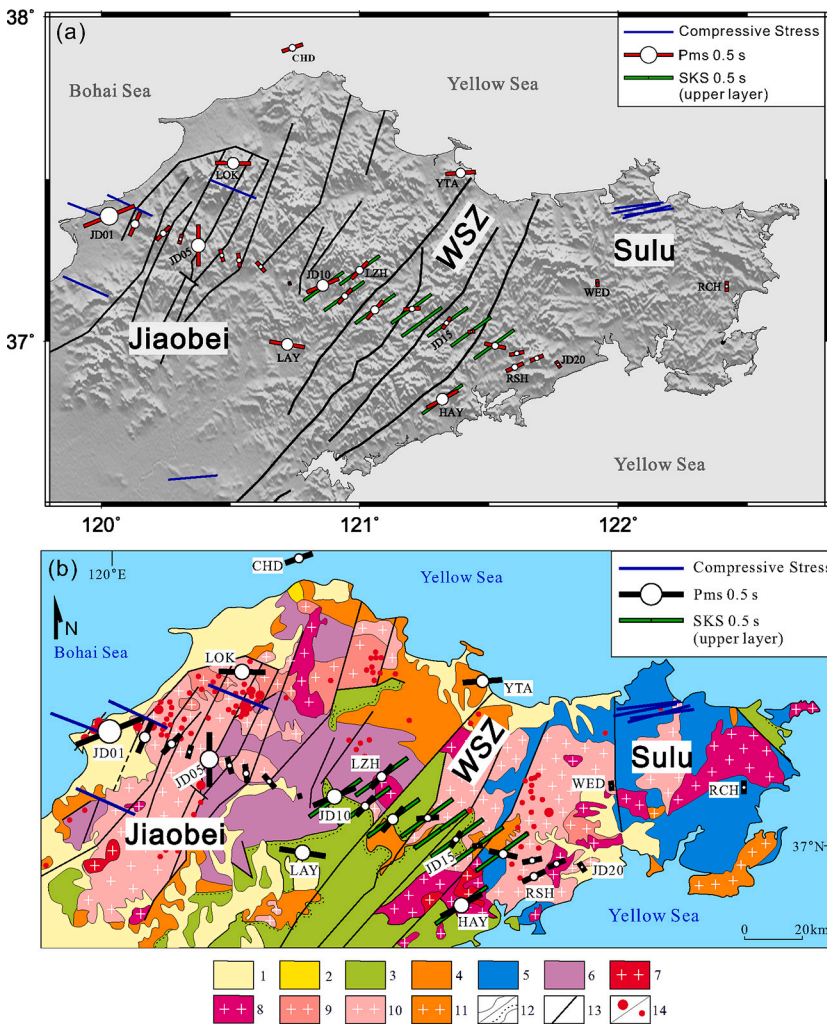
Fig. 9. (a) The estimated crust azimuthal anisotropy in this study. The red bars indicate the splitting parameters determined in this study with white circles whose radiuses are in proportion to the delay times. The green bars represent the upper layer anisotropy of the double-layer anisotropy pattern based on XKS splitting analysis (Wu et al., 2020). The blue bars represent the maximum horizontal compressive stress (S_Hmax) (Heidbach et al., 2018). (b) The estimated crust azimuthal anisotropy projected on the geological map (modified from Song, 2015; Yu et al., 2020a). 1, Quaternary loose sediments; 2, Paleogene-Neogene terrestrial volcanic-sedimentary strata; 3, Cretaceous continental volcanic-sedimentary strata; 4, Paleoproterozoic-Neoproterozoic shore-shallow marine facies strata; 5, Neoproterozoic with eclogite granitic gneiss; 6, Archean granite-greenstone belt; 7, Cretaceous Laoshan granite; 8, Cretaceous Weideshan Granite; 9, Cretaceous Guojialing granodiorite; 10, Jurassic granite; 11, Triassic granitoids; 12, conformity / unconformity; 13, fault; 14, large to super-large gold deposit / medium gold deposit. (For interpretation of the references to colour in this figure legend, the reader is referred to the web version of this article.)

References

Ammon, C.J., 1991. The isolation of receiver effects from teleseismic P waveforms. Bull. Seismol. Soc. Am. 81 (6), 2504–2510.
Boness, N.L., Zoback, M.D., 2006. Mapping stress and structurally controlled crustal shear velocity anisotropy in California. Geology 34 (10), 825–828.
Chen, L., 2010. Concordant structural variations from the surface to the base of the upper mantle in the North China Craton and its tectonic implications. Lithos 120 (1–2), 96–115.
Chen, L., Zheng, T., Xu, W., 2006. A thinned lithospheric image of the Tanlu Fault Zone, eastern China: constructed from wave equation based receiver function migration. J. Geophys. Res. Solid Earth 111 (B9).

Chen, Y., Zhang, Z., Sun, C., Badal, J., 2013. Crustal anisotropy from Moho converted Ps wave splitting analysis and geodynamic implications beneath the eastern margin of Tibet and surrounding regions. Gondwana Res. 24 (3–4), 946–957.
Cochran, E.S., Kroll, K.A., 2015. Stress-and structure-controlled anisotropy in a region of complex faulting—Yuha Desert, California. Geophys. J. Int. 202 (2), 1109–1121.
Crampin, S., 1991. Wave propagation through fluid-filled inclusions of various shapes: interpretation of extensive-dilatancy anisotropy. Geophys. J. Int. 104 (3), 611–623.
Faure, M., Lin, W., Le Breton, N., 2001. Where is the North China–South China block boundary in eastern China? Geology 29 (2), 119–122.
Frederiksen, A., Bostock, M., 2000. Modelling teleseismic waves in dipping anisotropic structures. Geophys. J. Int. 141 (2), 401–412.
Gao, Y., Wu, J., Fukao, Y., Shi, Y., Zhu, A., 2011. Shear wave splitting in the crust in North China: stress, faults and tectonic implications. Geophys. J. Int. 187 (2), 642–654.
Gilder, S.A., Leloup, P.H., Courtillot, V., Chen, Y., Coe, R.S., Zhao, X., Xiao, W., Halim, N., Cogné, J.P., Zhu, R., 1999. Tectonic evolution of the Tancheng-Lujiang (Tan-Lu) fault via middle Triassic to early Cenozoic paleomagnetic data. J. Geophys. Res. Solid Earth 104 (B7), 15365–15390.
Girardin, N., Farra, V., 1998. Azimuthal anisotropy in the upper mantle from observations ofP-to-S converted phases: application to Southeast Australia. Geophys. J. Int. 133, 615–629.
Guo, G., Zhang, Z., Cheng, J., Dong, Y., Yan, J., Ma, Y., 2015. Seismic anisotropy in the crust in northeast margin of Tibetan Plateau and tectonic implication. Chin. J. Geophys. 58 (11), 4092–4105 (in Chinese).
Hacker, B.R., Ratschbacher, L., Webb, L., Ireland, T., Walker, D., Shuwen, D., 1998. U/Pb zircon ages constrain the architecture of the ultrahigh-pressure Qinling–Dabie Orogen, China. Earth Planet. Sci. Lett. 161 (1–4), 215–230.
Hacker, B.R., Ratschbacher, L., Webb, L., McWilliams, M.O., Ireland, T., Calvert, A., Dong, S., Wenk, H.R., Chateigner, D., 2000. Exhumation of ultrahigh-pressure continental crust in east central China: Late Triassic-Early Jurassic tectonic unroofing. J. Geophys. Res. Solid Earth 105 (B6), 13339–13364.
Heidbach, O., Rajabi, M., Cui, X., Fuchs, K., Müller, B., Reinecker, J., Reiter, K., Tingay, M., Wenzel, F., Xie, F., 2018. The World Stress Map database release 2016: Crustal stress pattern across scales. Tectonophysics 744, 484–498.

Kennett, B., Engdahl, E., 1991. Traveltimes for global earthquake location and phase identification. Geophys. J. Int. 105 (2), 429–465.

Kong, F., Wu, J., Liu, K.H., Gao, S.S., 2016. Crustal anisotropy and ductile flow beneath the eastern Tibetan Plateau and adjacent areas. Earth Planet. Sci. Lett. 442, 72–79.

Li, C., Chen, C., Dong, D., Kuponiyi, A.P., Dosso, S.E., Su, D., 2018. Ambient noise tomography of the Shandong province and its implication for Cenozoic intraplate volcanism in eastern China. Geochem. Geophys. Geosyst. 19 (9), 3286–3301.

Li, J., Song, X., Wang, P., Zhu, L., 2019. A generalized H-κ method with harmonic corrections on Ps and its crustal multiples in receiver functions. J. Geophys. Res. Solid Earth 124, 3782–3801.

Li, Z., Peng, Z., 2017. Stress- and structure-induced anisotropy in Southern California from two decades of shear wave splitting measurements. Geophys. Res. Lett. 44 (19), 9607–9614.

Lin, W., Wei, W., 2020. Late Mesozoic extensional tectonics in the North China Craton and its adjacent regions: a review and synthesis. Int. Geol. Rev. 62 (7–8), 811–839.

Lin, W., Ji, W., Shi, Y., Chu, Y., Li, Q., Chen, Z., Liu, F., Wang, Q., 2013. Multi-stage exhumation processes of the UHP metamorphic rocks: Implications from the extensional structure of Tongbai-Hong'an-Dabieshan orogenic belt. Chin. Sci. Bull. 58, 2259–2265.

Liu, H., Niu, F., 2012. Estimating crustal seismic anisotropy with a joint analysis of radial and transverse receiver function data. Geophys. J. Int. 188 (1), 144–164.

Liu, Z., Park, J., 2017. Seismic receiver function interpretation: Ps splitting or anisotropic underplating? Geophys. J. Int. 208, 1332–1341.

Liu, Z., Park, J., Rye, D.M., 2015. Crustal anisotropy in the northeastern Tibetan Plateau inferred from receiver functions: Rock textures caused by metamorphic fluids and lower crust flow? Tectonophysics 661, 66–80.

Mao, J., Wang, Y., Li, H., Pirajno, F., Zhang, C., Wang, R., 2008. The relationship of mantle-derived fluids to gold metallogenesis in the Jiaodong Peninsula: evidence from D–O–C–S isotope systematics. Ore Geol. Rev. 33 (3–4), 361–381.

Meng, L., Lin, W., 2021. Episodic crustal extension and contraction characterizing the Late Mesozoic tectonics of East China: Evidence from the Jiaodong Peninsula, East China. Tectonics 40 e2020TC006318.

Niu, F., Li, J., 2011. Component azimuths of the CEArray stations estimated from P-wave particle motion. Earthq. Sci. 24 (1), 3–13.

Okay, A.I., Celal Şengör, A., 1992. Evidence for intracontinental thrust-related exhumation of the ultra-high-pressure rocks in China. Geology 20 (5), 411–414.

Pan, S., Wang, F., Zheng, Y., Duan, Y., Liu, L., Deng, X., Song, X., Sun, Y., Ma, C., Li, Y., 2015. Crustal velocity structure beneath Jiaodong peninsula and its tectonic implications. Chin. J. Geophys. 58 (9), 3251–3263 (in Chinese).

Peng, Z., Ben-Zion, Y., 2004. Systematic analysis of crustal anisotropy along the Karadere—Düzce branch of the North Anatolian fault. Geophys. J. Int. 159 (1), 253–274.

Qiang, Z., Wu, Q., Li, Y., He, J., Gao, M., 2016. Crustal anisotropy beneath central-south Mongolia and its dynamic implications. Chin. J. Geophys. 59 (5), 1616–1628 (in Chinese).

Qiang, Z., Wu, Q., He, J., Li, Y., 2019. Crustal azimuthal anisotropy beneath Abag area in Inner Mongolia, China. Chin. J. Geophys. 62 (8), 2946–2958 (in Chinese).

Rümpker, G., Kaviani, A., Latifi, K., 2014. Ps-splitting analysis for multilayered anisotropic media by azimuthal stacking and layer stripping. Geophys. J. Int. 199 (1), 146–163.

Savage, M., 1999. Seismic anisotropy and mantle deformation: what have we learned from shear wave splitting? Rev. Geophys. 37 (1), 65–106.

Shen, X., Yuan, X., Ren, J., 2015. Anisotropic low–velocity lower crust beneath the northeastern margin of Tibetan Plateau: Evidence for crustal channel flow. Geochem. Geophys. Geosyst. 16 (12), 4223–4236.

Shi, Y., Gao, Y., Tai, L., Fu, Y., 2015. The shear-wave splitting in the crust and the upper mantle around the Bohai Sea, North China. J. Asian Earth Sci. 111, 505–516.

Song, M.C., 2015. The may achievements and key theory and methods of deep-seated prospecting in the Jiaodong gold concentration area, Shandong Province. Geol. Bull. China 34 (9), 1758–1771 (in Chinese with English abstract).

Sun, Y., Niu, F., Liu, H., Chen, Y., Liu, J., 2012. Crustal structure and deformation of the SE Tibetan plateau revealed by receiver function data. Earth Planet. Sci. Lett. 349, 186–197.

Tang, J., Zheng, Y.-F., Wu, Y.-B., Gong, B., Zha, X., Liu, X., 2008. Zircon U–Pb age and geochemical constraints on the tectonic affinity of the Jiaodong terrane in the Sulu orogen, China. Precambrian Res. 161 (3–4), 389–418.

Tian, X., Santosh, M., 2015. Fossilized lithospheric deformation revealed by teleseismic shear wave splitting in eastern China. GSA Today 25 (2), 4–10.

Wang, P., Huang, Z., Wang, X., 2020. A method for estimating the crustal azimuthal anisotropy and Moho orientation simultaneously using receiver functions. J. Geophys. Res. Solid Earth 125 e2019JB018405.

Wang, Q., Niu, F., Gao, Y., Chen, Y., 2016. Crustal structure and deformation beneath the NE margin of the Tibetan plateau constrained by teleseismic receiver function data. Geophys. J. Int. 204 (1), 167–179.

Wu, C., Tian, X., Xu, T., Liang, X., Chen, Y., Taylor, M., Badal, J., Bai, Z., Duan, Y., Yu, G., 2019a. Deformation of crust and upper mantle in central Tibet caused by the northward subduction and slab tearing of the Indian lithosphere: New evidence based on shear wave splitting measurements. Earth Planet. Sci. Lett. 514, 75–83.

Wu, C., Tian, X., Xu, T., Liang, X., Chen, Y., Zhu, G., Badal, J., Bai, Z., Yu, G., Teng, J., 2019b. Upper-crustal anisotropy of the conjugate strike-slip fault zone in Central Tibet analyzed using local earthquakes and shear-wave splitting. Bull. Seismol. Soc. Am. 109 (5), 1968–1984.

Wu, C., Xu, T., Ai, Y., Dong, W., Li, L., 2020. XKS splitting-based upper-mantle deformation in the Jiaodong Peninsula records the boundary between the North China Craton and South China Block. Geophys. J. Int. 222 (2), 956–964.

Wu, Y.B., Zheng, Y.F., Zhou, J.B., 2004. Neoproterozoic granitoid in northwest Sulu and its bearing on the North China–South China Blocks boundary in east China. Geophys. Res. Lett. 31 (7).

Yang, H., Badal, J., Hu, J., Peng, H., 2019. Disaggregated anisotropy and deformation style of the upper and lower crust in the southeastern Tibetan plateau. J. Asian Earth Sci. 184, 103999.

Yang, J., Chu, M., Liu, W., Zhai, M., 2003b. Geochemistry and petrogenesis of Guojialing granodiorites from the northwestern Jiaodong Peninsula, eastern China. Acta Petrol. Sin. 19 (4), 692–700.

Yang, J., Zhao, L., Kaus, B.J., Lu, G., Wang, K., Zhu, R., 2018a. Slab-triggered wet upwellings produce large volumes of melt: Insights into the destruction of the North China Craton. Tectonophysics 746, 266–279.

Yang, J.-H., Wu, F.-Y., Wilde, S.A., 2003a. A review of the geodynamic setting of large-scale Late Mesozoic gold mineralization in the North China Craton: an association with lithospheric thinning. Ore Geol. Rev. 23 (3–4), 125–152.

Yang, J.-H., Wu, F.-Y., Chung, S.-L., Wilde, S.A., Chu, M.-F., Lo, C.-H., Song, B., 2005. Petrogenesis of Early Cretaceous intrusions in the Sulu ultrahigh-pressure orogenic belt, east China and their relationship to lithospheric thinning. Chem. Geol. 222 (3–4), 200–231.

Yang, Q.-Y., Santosh, M., 2015. Early Cretaceous magma flare-up and its implications on gold mineralization in the Jiaodong Peninsula, China. Ore Geol. Rev. 65, 626–642.

Yang, Y., Yao, H., Zhang, P., Chen, L., 2018b. Crustal azimuthal anisotropy in the trans-North China orogen and adjacent regions from receiver functions. Sci. China Earth Sci. 61 (7), 903–913.

Yu, G., Xu, T., Ai, Y., Chen, L., Yang, J., 2020a. Significance of crustal extension and magmatism to gold deposits beneath Jiaodong Peninsula, eastern North China Craton: Seismic evidence from receiver function imaging with a dense array. Tectonophysics 789, 228532.

Yu, G., Xu, T., Liu, J., Ai, Y., 2020b. Late Mesozoic extensional structures and gold mineralization in Jiaodong Peninsula, eastern Northern China Craton: an inspiration from ambient noise tomography on data from a dense seismic array. Chin. J. Geophys. 63 (5), 1878–1893 (in Chinese).

Zhai, M., Cong, B., Guo, J., Liu, W., Li, Y., Wang, Q., 2000. Sm-Nd geochronology and petrography of garnet pyroxene granulites in the northern Sulu region of China and their geotectonic implication. Lithos 52 (1–4), 23–33.

Zhang, K., Lü, Q., Yan, J., Hu, H., Fu, G., Shao, L., 2018. Crustal structure beneath the Jiaodong Peninsula, North China, revealed with a 3D inversion model of magnetotelluric data. J. Geophys. Eng. 15 (6), 2442–2454.

Zhang, Y., Li, J., Zhang, T., Yuan, J., 2007. Late Mesozoic kinematic history of the Muping-Jimo fault zone in Jiaodong Peninsula, Shandong Province, East China. Geol. Rev. 53 (3), 289–300.

Zheng, T., Zhao, L., Xu, W., Zhu, R., 2008. Insight into modification of North China Craton from seismological study in the Shandong Province. Geophys. Res. Lett. 35 (22).

Zheng, T., Ding, Z., Ning, J., Liu, K.H., Gao, S.S., Chang, L., Kong, F., Fan, X., 2019. Crustal azimuthal anisotropy beneath the central North China Craton revealed by receiver functions. Geochem. Geophys. Geosyst. 20 (5), 2235–2251.

Zheng, X.-F., Yao, Z.-X., Liang, J.-H., Zheng, J., 2010. The role played and opportunities provided by IGP DMC of China National Seismic Network in Wenchuan earthquake disaster relief and researches. Bull. Seismol. Soc. Am. 100 (5B), 2866–2872.

Zheng, Y.-F., Zhou, J.-B., Wu, Y.-B., Xie, Z., 2005. Low-grade metamorphic rocks in the Dabie-Sulu orogenic belt: A passive-margin accretionary wedge deformed during continent subduction. Int. Geol. Rev. 47 (8), 851–871.

Zhou, J.-B., Wilde, S.A., Zhao, G.-C., Zheng, C.-Q., Jin, W., Zhang, X.-Z., Cheng, H., 2008. SHRIMP U-Pb zircon dating of the Neoproterozoic Penglai Group and Archean gneisses from the Jiaobei Terrane, North China, and their tectonic implications. Precambrian Res. 160 (3–4), 323–340.

Zhu, G., Wang, D., Liu, G., Niu, M., Song, C., 2004. Evolution of the Tan-Lu fault zone and its responses to plate movements in west Pacific basin. Chin. J. Geol. 39 (1), 36–49.

Zhu, R., Zheng, T., 2009. Destruction geodynamics of the North China Craton and its Paleoproterozoic plate tectonics. Chin. Sci. Bull. 54 (19), 3354.